

Global diagnostics of ionospheric absorption during X-ray solar flares based on 8-20MHz noise measured by over-the-horizon radars.

Berngardt O.I. Ruohoniemi J.M. St-Maurice J.-P.
 Marchaudon A. Kosch M.J. Yukimatu A.S.
 Nishitani N. Shepherd S.G. Marcucci M.F. Hu H.
 Nagatsuma T. Lester M.

December 24, 2018

Abstract

An analysis of noise attenuation during eighty solar flares between 2013 and 2017 was carried out at frequencies 8-20 MHz using thirty-four SuperDARN radars and the EKB ISTP SB RAS radar. The attenuation was determined on the basis of noise measurements performed by the radars during the intervals between transmitting periods. The location of the primary contributing ground sources of noise was found by consideration of the propagation paths of radar backscatter from the ground. The elevation angle for the ground echoes was determined through a new empirical model. It was used to determine the paths of the noise and the location of its source. The method was particularly well suited for daytime situations which had to be limited for the most part to only two crossings through the D region. Knowing the radio path was used to determine an equivalent vertical propagation attenuation factor. The change in the noise during solar flares was correlated with solar radiation lines measured by GOES/XRS, GOES/EUVS, SDO/AIA, SDO/EVE, SOHO/SEM and PROBA2/LYRA instruments. Radiation in the 1 to 8Å and near 100Å are shown to be primarily responsible for the increase in the radio noise absorption, and by inference, for an increase in the D and E region density. The data are also shown to be consistent with a radar frequency dependence having a power law with an exponent of -1.6. This study shows that a new dataset can be made available to study D and E region.

1 Introduction

The monitoring of ionospheric absorption at High Frequency (HF), particularly at high latitudes, makes it feasible to predict radio wave absorption at long distances and therefore on global scales (DRAP Documentation, 2010; Akmaev, R. A., 2010). This in turn makes it a useful tool for study of the dynamics of the D and E regions. Traditionally, there are several techniques in use (Davies, 1969; Hunsucker & Hargreaves, 2002), including constant power 2-6 MHz transmitters (URSI A1 and A3 methods, see for example (Sauer & Wilkinson, 2008;

Schumer, 2010)), riometry using cosmic radio space sources at 30-50 MHz (URSI A2 method (Hargreaves, 2010)) and imaging riometry (Detrick & Rosenberg, 1990). Recently, a large, spatially distributed network of riometers has been deployed to monitor absorption (Rogers & Honary, 2015). The development of new techniques for studying absorption with wide spatial coverage would be valuable for the validation of global ionospheric models and for global absorption forecasting.

A wide network of radio instruments in the HF frequency range is available with the SuperDARN (Super Dual Auroral Radar Network (Greenwald et al., 1995; Chisham et al., 2007)) radars and radars close to them in terms of design and software (Berngardt, Zolotukhina, & Oinats, 2015). The main task of the SuperDARN network is to measure ionospheric convection. Currently this network is expanding from polar latitudes to mid-latitudes (J. Baker et al., 2007; Ribeiro et al., 2012) and possibly to equatorial latitudes (Lawal et al., 2018). Regular radar operation with high spatial and temporal resolutions and a wide field-of-view makes them a useful tool for monitoring ionospheric absorption on global scales. The frequency range used by the radars fills a gap between the riometric measurements at 30-50 MHz (URSI A2 method) and radar measurements at 2-6 MHz band (URSI A1, A3 methods). Various methods are being developed for using these radars to study radiowave absorption. One approach is to monitor third-party transmitters (Squibb et al., 2015) and another is to use the signal backscattered from the ground (Watanabe & Nishitani, 2013; Chakraborty, Ruohoniemi, Baker, & Nishitani, 2018; Fiori et al., 2018). In this paper, another method is investigated. It is based on studying the attenuation of HF noise in the area surrounding the radar that is measured without transmitting any sounding pulses.

Every several seconds, before transmitting at the operating frequency, the radar measures the spectrum of the background noise in a 300-500 kHz band centered on a planned operating frequency that lies between 8-20 MHz. The minimum in the spectral intensity is recorded and defined here as the 'minimal HF noise level'.

(Berngardt et al., 2018) showed that the dynamics of the minimal HF noise level is strongly influenced by X-ray 1-8Å solar radiation in the daytime. This effect has also been observed during solar proton events (Bland, Heino, Kosch, & Partamies, 2018) where it was found to correlate well with riometer observations. This allows one to use the noise measured with HF radars to investigate the absorption processes in the lower part of the ionosphere in passive mode, without the use of third-party transmitters, and without relying on the presence of backscatter from the ground.

To use this new technique on a regular basis for monitoring ionospheric absorption we should investigate the observed noise level variations during X-ray flares and show that the observed dynamics are consistent with the current absorption models.

As shown in the preliminary analysis (Berngardt et al., 2018), there is significant correlation of noise level attenuation with the intensity of X-ray solar radiation in the range 1-8Å. However, the temporal dynamics of the absorption sometimes do not precisely track the solar radiation at wavelengths of 1-8Å, which indicates the presence of mechanisms other than the ionization of the D-layer by 1-8Å solar radiation. An example of such a comparison will be presented here in Fig.1A-D and was shown by (Berngardt et al., 2018, fig.9).

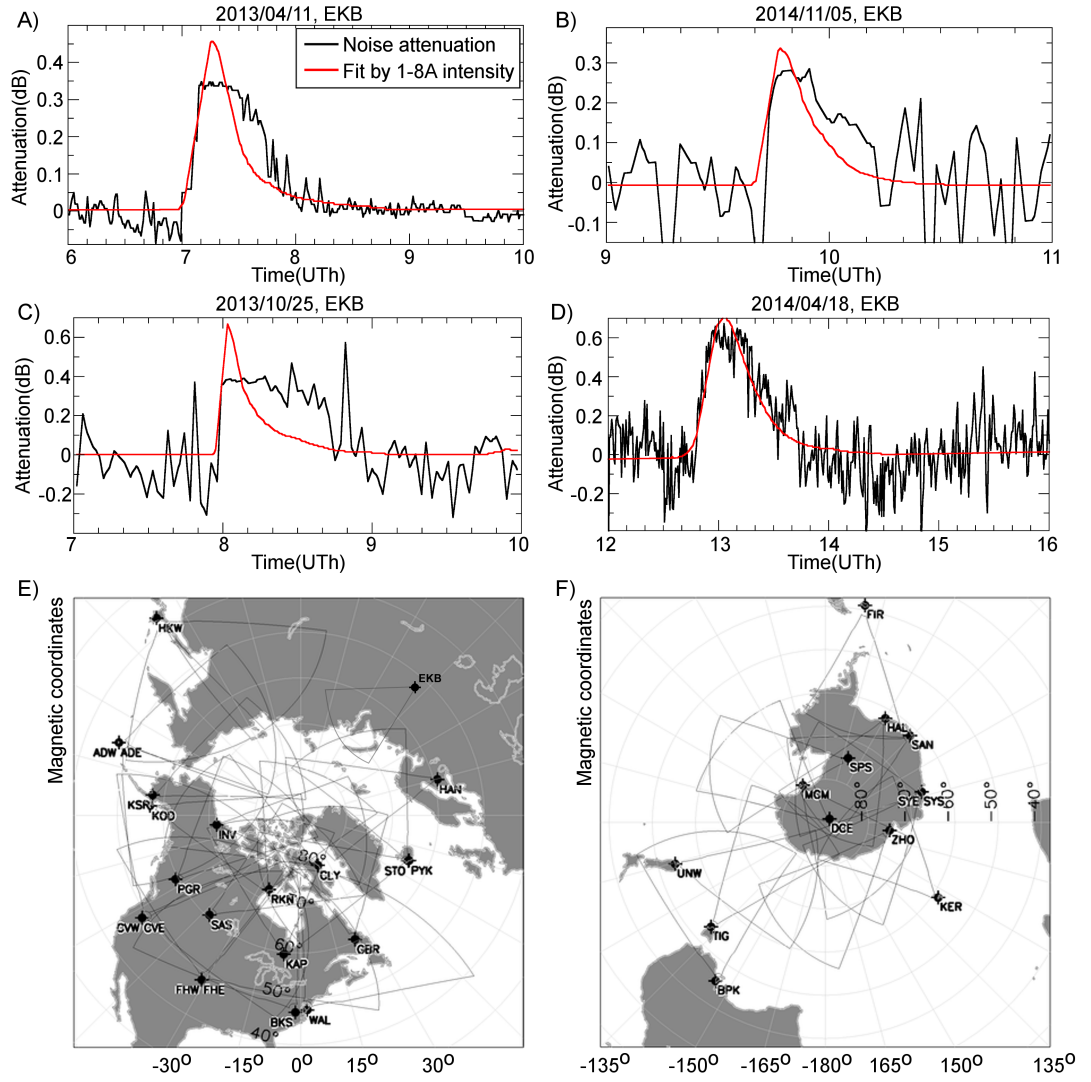


Figure 1: A-D) comparison of the X-ray intensity dynamics measured on GOES/XRS 1-8Å and the noise attenuation at EKB ISTP SB RAS radar during four flares; E-F) - fields of views of radars that participated in the work

In contrast to riometers which measure ionospheric absorption at relatively high frequencies (30-50 MHz), the SuperDARN coherent radars use lower operating frequencies and ionospheric refraction significantly affects the absorption level - the trajectory of propagation is distorted by the background ionosphere. To compare the data of different radars during different solar flares, our method requires taking into account the state of the background ionosphere during each experiment. This allows an oblique absorption measurement to be converted to an equivalent vertical measurement. In addition, the solution of this problem allows determination of the geographic location of the region in which the absorption takes place.

Among the factors that affect the error in estimating the absorption level is the frequency at which the radar operates and its irregular switching. It is known that the absorption of radio waves depends on frequency, but this dependence is taken into account in different ways in different papers. In order to make a reliable comparison of data collected from radars operating at different frequencies, it is necessary to find the frequency dependence of the HF noise absorption, and to take it into account. This will allow us to infer the absorption at any frequency from the observed absorption at the radar operating frequency.

The third factor that needs to be taken into account is the altitude localization of the absorption.

The present paper is devoted to solving these problems. An analysis is made of 80 X-ray solar flares during the years 2013-2017, which were also considered in (Berngardt et al., 2018) based on the available data of 34 high- and mid-latitude radars of SuperDARN network and on the EKB ISTP SB RAS (Berngardt et al., 2015) radar data. The radar locations and their fields of view are shown in fig.1E-F, the radar coordinates are given in the Table ???. The X-ray solar flares dates are listed in (Berngardt et al., 2018).

2 Taking into account the background ionosphere

As was shown in (Berngardt et al., 2018), during solar X-ray flares attenuation of the minimal noise level in the frequency range 8-20 MHz is observed on the dayside by midlatitude coherent radars. The attenuation correlates with the increase of X-ray solar radiation $1-8\text{\AA}$ and is associated with the absorption of the radio signal in the lower part of the ionosphere.

The HF radio noise intensity is known to vary with local time due different sources (ITU-R P.372-13, 2016). At night, the noise is mostly atmospheric, and is formed by long-range propagation from noise sources around the world, mostly from regions of thunderstorm activity. In the daytime the atmospheric noise level significantly decreases due to regular absorption in the lower part of the ionosphere and the increasing number of propagation hops (caused by increasing electron density and lowering of the radiowave reflection point). As a result, in the daytime the multihop propagation part of the noise becomes small, and only noise sources from the first propagation hop (mostly anthropogenic noise) need to be taken into account (Berngardt et al., 2018).

An important issue related to the interpretation of the noise level is the spatial localization of the effect. It can be estimated by taking into account the radiowave trajectory along which most of the noise is received and absorption is taking place. We will argue that ionization of the lower ionosphere is

small enough and skip distance variability is less pronounced than the variations caused by other regular and irregular ionospheric variations.

Let us consider the problem of detecting the noise source from the data of a HF coherent radar. It is known that the intensity of the signal transmitted by an isotropic source and propagating in an inhomogeneous ionosphere substantially depends on the ground distance from the signal transmitter to receiver. If we consider only waves reflecting from the ionosphere, then at sounding frequencies above f_oF2 there is a spatial region where the signal cannot be received - the dead zone. At the boundary of this dead zone (skip distance) the signal appears and is significantly enhanced compared to other distances (Shearman, 1956; Bliokh, Galushko, Minakov, & Yampolski, 1988).

More specifically, consider that, due to refraction, the signal transmitted by a point source produces a non-uniform distribution of power $P(x)$ over the range x . According to the theory of radio wave propagation, the distribution of signal power is determined by the spatial focusing of the radio wave in the ionosphere, and has a sharp peak at the boundary of the dead zone (Kravtsov & Orlov, 1983). According to (Tinín, 1983) in a plane-layered ionosphere, the distribution of the power over range is:

$$P(x) \simeq \frac{1}{\sqrt{\sigma_x(s_m)\bar{x}''(s_m)}} e^{-\frac{\xi^2}{4}} D_{-\frac{1}{2}}(\xi) \quad (1)$$

where $D_{-\frac{1}{2}}(\xi)$ is the parabolic cylinder function (Weisstein, n.d.); x_m - the distance at which the spatial focusing is observed; $\xi = \frac{x_m - x}{\sigma_x(s_m)}$ is the normalized range relative to x_m ; s_m is the sine of elevation angle; $\sigma_x(s_m)$ is the standard deviation of x over the geometric optical rays; \bar{x}'' is second differential of x with respect to s_m .

Let us consider this signal after it is scattered by inhomogeneities on the Earth's surface and then received by the radar. In the first approximation the power of the signal received by the radar will be proportional to the product of (i) the power of the incident signal $P(x)$ (related to spatial focusing when propagating from the radar to the Earth's surface); (ii) the scattering cross-section $\sigma(x)$ (related to inhomogeneities of the Earth's surface); and (iii) the incident power $P(x)$ (related to the propagation from the Earth's surface to the radar).

This signal is received as a powerful signal coming from a small range of distances. When analyzing the data of coherent HF radars, this signal, associated with the focusing of the radio wave at the boundary of the dead zone, is referred to as ground scatter (GS) (Shearman, 1956).

The scattering cross section $\sigma(x)$ essentially depends on the angles of incidence and reflection of the wave, as well as on the properties and geometry of the scattering surface. This causes a significant dependence of the GS signal on the landscape and the season (Ponomarenko, St.-Maurice, Hussey, & Koustov, 2010). In the case of presence of significant inhomogeneities, for example, mountains (Uryadov, Vertogradov, Sklyarevsky, & Vybornov, 2018), $\sigma(x)$ may cause the appearance of additional maxima and minima in the GS signal. For relatively homogeneous surfaces, the position of the GS maximum remains almost unchanged, and the GS signal propagation trajectory (radar-surface-radar) can be used to estimate the trajectory of the propagation of the noise signal (surface-radar). Below we use this approximation to localize noise source using GS signal

properties.

Let the independent noise sources be distributed over the Earth's surface over the distance x of the first hop (from 0 to 3000km). Let their intensity be $B(x)$ and the radiation pattern of each of them be nearly isotropic over the elevation angles forming the GS signal. Let the noise signals interfere incoherently. In this case the power of the signal $P_0(x_1)$, received at the point $x = x_1$, in the first approximation becomes:

$$P_0(x_1) \simeq \int_{-\infty}^{\infty} B(x)P(x_1 - x)dx \quad (2)$$

Thus, one can represent the formation of the noise power from terrestrial sources, as a weighted sum of the contributions from individual noise sources. The function $P(x)$ is the weight, and the region of localization of the noise source is of the order of the maximal width of the GS signal (see equation 1). According to the experimental data it is of the order of several hundred kilometers. For the validity of equation (2), the characteristic scale of the homogeneity of the ionosphere in the horizontal direction should be about the width of the GS signal maximum. The process of forming the received signal is illustrated in Fig.2B.

Thus, the problem of localization of the noise source can be reduced to determining the geographic location of the region forming the GS signal and determining the propagation path of the signal from this region to the receiver.

In radar techniques, there are a number of procedures for separating the GS signal from other scattered signal types (K. B. Baker, Greenwald, Villian, & Wing, 1988; Barthes, Andre, Cerisier, & Villain, 1998; Blanchard, Sundeen, & Baker, 2009; Ribeiro et al., 2011; Liu, Hu, Liu, Wu, & Lester, 2012), but using them for automatic location of the effective noise source causes some problems. To begin with the GS signal can have several ranges at one time (for example first-hop GS and second-hop GS, or multimode propagation due to mid-scale irregularities (Stocker, Arnold, & Jones, 2000)). It may be discontinuous in time due to defocusing (refraction) and absorption processes. Finally, it may have irregular temporal dynamics due to large scale ionospheric variations (for example, internal atmospheric waves (Oinats, Nishitani, Ponomarenko, Berngardt, & Ratovsky, 2016; Stocker et al., 2000)). These problems significantly complicate the automatic interpretation of the radar data for our task, especially for high-latitude radars where the ionosphere is essentially heterogeneous with latitude. Therefore, for automatic estimation of the effective noise location, it was decided to use a smooth adaptive model of GS position, automatically corrected by the experimental data.

The study of absorption on the long paths using GS signal or noise requires knowledge of the trajectory of radio space signal propagation especially in the two regions where it intersects the D-layer - near the receiver (radar) and near the transmitter source (point of focusing, where the GS signal is formed). According to the Breit-Tuве principle (Davies, 1969), it is sufficient to know the angle of arrival of the GS signal and the radar range. In practice, however, there are two significant problems: the separation of the GS signal from the ionospheric scatter (IS) signal (Blanchard et al., 2009; Ribeiro et al., 2011) and the calibration of the arrival angle measurements (Ponomarenko, Nishitani, Oinats, Tsuya, & St.-Maurice, 2015; Shepherd, 2017; Chisham, 2018).

Fig.2C-H presents examples of the location of signals detected as GS by the standard FitACF algorithm (used on these radars for signal processing). It can

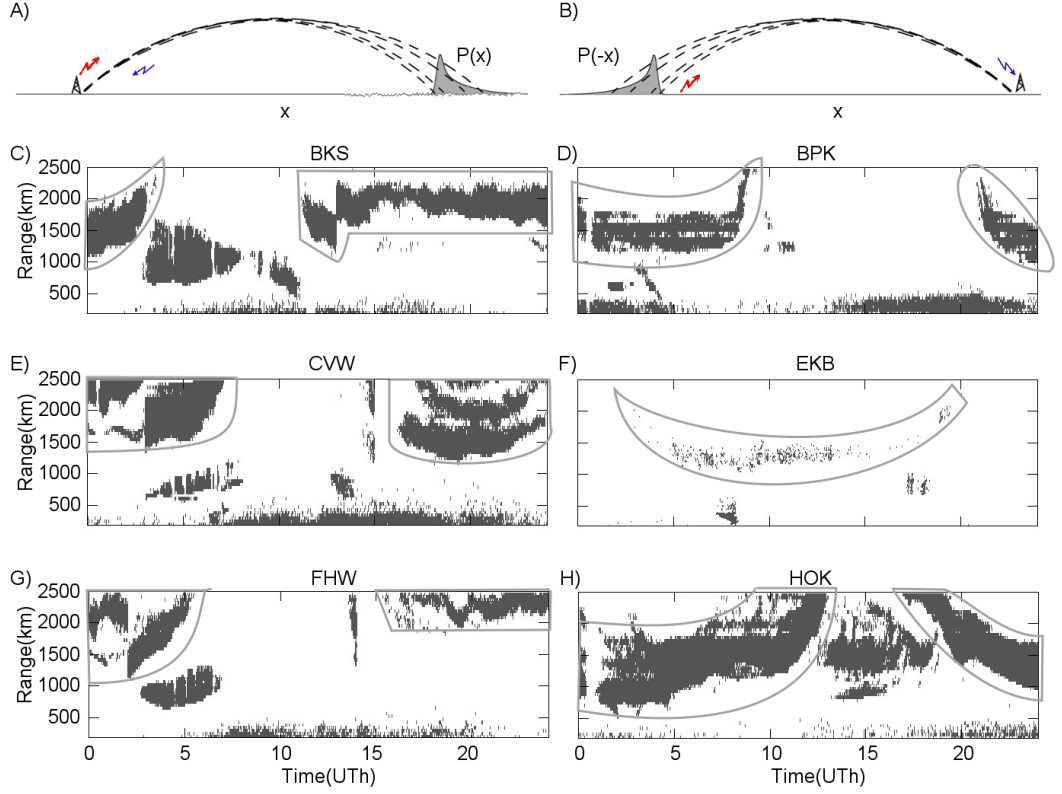


Figure 2: A) - formation of GS signal; B) - formation of noise power level by distribution of noise sources. Red and blue arrows in A-B) mark transmitted and received signals; C-H) - the position of the signals, defined by FitACF algorithm as GS, during 18/04/2016 on the radars BKS, BPK, CVW, EKB, FHW, HOK. Gray enclosed areas correspond to GS when focusing in the F-layer. Other areas are defined by the algorithm, as GS, but having, sometimes, an ionospheric origin.

be seen from the figure that the scattered signal can include several propagation paths (Fig.2E, 16-24UT), variations in the GS signal range (associated, for example, with the propagation of internal atmospheric waves (Stocker et al., 2000; Oinats et al., 2016) (Fig.2C, 14-18UT ; Fig.2G, 18-21UT)), as well as ionospheric and meteor trail scattering (Fig.2C-H, ranges below 400km)(Hall et al., 1997; Yukimatu & Tsutsumi, 2002; Ponomarenko, Iserhienrhien, & St.-Maurice, 2016). The signal that qualitatively corresponds to F-layer GS is marked at Fig.2C-H by enclosed regions (the modeling results demonstrating this will be shown later in the paper). These examples demonstrate that the problem of stable and automatic selection of the GS region associated with reflection from the F-layer is rather complicated even with use of the standard processing techniques.

In this study, the position of the F-layer GS signal was solved for each radar beam separately and independently. To generate input data for the GS

positioning algorithm for each moment we identify the ranges where the signals have the maximum amplitude in the radar data. For this purpose we select only signals determined by the standard FitACF algorithm to be GS signal.

Using these prepared input data, we determine the smooth curve of the distribution of GS with range, within the framework of an empirical ionospheric model with a small number of parameters, adapted to the experimental data. The problem of determining the position of the GS signal causes certain difficulties connected to the presence of a large number of possible focusing points associated with the heterogeneity of the ionosphere along the signal propagation path (Stocker et al., 2000) and ionospheric scattered signals incorrectly identified as GS signals.

For an approximate single-valued solution of this problem, we reformulate the problem as the problem of producing a GS signal in a plane-layered ionosphere with a parabolic layer with parameters estimated from the GS signal. In the framework of the plane-layered ionosphere with a parabolic F-layer, we have the following expression for the radar range to the boundary of the dead zone (Chernov, 1971):

$$R_{model} = \frac{f_0}{f_{oF2}} \left\{ 2h_{mF2}\sqrt{\chi} + \Delta h \cdot \ln \left(\frac{1 + \sqrt{\chi}}{1 - \sqrt{\chi}} \right) \right\} \quad (3)$$

where $\chi = \frac{h_{mF2} - \Delta h}{h_{mF2}}$; $h_{min} = h_{mF2} - \Delta h$ - is the minimal height of the ionosphere, obtained from the condition $N_e(h_{min}) = 0$; h_{mF2} is the height of the electron density maximum in the ionosphere, obtained from the condition $N_e(h_{mF2}) = max$; f_{oF2} is the plasma frequency of the F2 layer; f_0 is the carrier frequency of the sounding signal.

In this model, the geometric distance D over the Earth surface to the point of focusing is defined as (Chernov, 1971):

$$D_{model} = R_{model} \cos(\Theta_{model}) \quad (4)$$

The elevation angle Θ_{model} of the signal arriving from the dead zone boundary according to this model is calculated as:

$$\cos(\Theta_{model}) = \sqrt{1 - \chi \left(\frac{f_0}{f_{oF2}} \right)^{-2}} \quad (5)$$

For interpretation of absorption the elevation angle is very important: in the model of the plane-layered ionosphere it also corresponds to the elevation angle in the D-layer, and relates the observed absorption to absorption of vertically propagating radio space signal. So, this angle is important for the interpretation of absorption, both in the case of observing GS (Watanabe & Nishitani, 2013; Chakraborty et al., 2018; Fiori et al., 2018) and in the case of minimal noise analysis (Berngardt et al., 2018; Bland et al., 2018). Most of the radars do measure the elevation angle. However, since many antenna characteristics in the HF range vary with time it is very important to calibrate the angle. This should be performed on each radar separately and regularly (Ponomarenko et al., 2015; Chisham, 2018; Shepherd, 2017) and requires significant computations. To simplify the problem of smooth and continuous calculation of the GS elevation, we decided to use model calculations of the angle based on propagation in the adapted ionosphere model. In this sense this method is close to the

approach used in (Ponomarenko et al., 2015). One needs to just choose a proper ionospheric model.

The reference ionospheric model IRI (Bilitza et al., 2017) is a median model and sufficiently smooth in time, but by default it does not correctly describe fast changes of f_oF2 in some situations, especially at high latitudes (Blagoveshchenskii, Maltseva, Anishin, Rogov, & Sergeeva, 2015). This problem becomes especially critical for GS signal range calculations for sunset and sunrise periods. Searching for one or several IRI parameters that are constant during the day will not solve the problem, so it is necessary to use either an adaptive model that more adequately describes these periods, or to use IRI model corrected for each moment using data from an ionosonde network (Galkin, Reinisch, Huang, & Bilitza, 2012; Blagoveshchenskii et al., 2015). We use an adaptive model, which is easier to implement and does not require additional data and instruments.

The adaptive model of the parabolic-layer ionosphere was used with a non-linear model for $f_oF2(t)$ and constant values for h_{mF2} and Δh :

$$f_oF2(t) = f_{oF2,min} + (f_{oF2,max} - f_{oF2,min}) \varepsilon(t) \quad (6)$$

$$\varepsilon(t) = \frac{\text{atan}(\beta \cdot (\Theta(t - \Delta T) - \alpha)) - \text{atan}(\beta \cdot (\Theta_{min} - \alpha))}{\text{atan}(\beta \cdot (\Theta_{max} - \alpha)) - \text{atan}(\beta \cdot (\Theta_{min} - \alpha))} \quad (7)$$

where $\Theta(t)$ is the cosine of the solar zenith angle at the radar location as a function of the time t ; $\Theta_{min}, \Theta_{max}$ is the maximal and minimal cosine of the solar zenith angle during the day; $\alpha, \beta, \Delta T$ are modeled parameters, computed during the fitting procedure. More correctly solar zenith angle should be calculated at the point of radiowave absorption but in this paper we do not use this. The parameter ΔT compensates the difference in the first approximation.

The required strong nonlinearity of the model during sunset and sunrise moments is provided by the $\text{atan}()$ function, by the cosine of the solar zenith angle $\Theta(t)$ and controlled by several parameters: $\alpha, \beta, \Delta T, f_{oF2,max}, f_{oF2,min}$. The model has enough degrees of freedom to describe the fast dynamics of $f_oF2(t)$ during solar terminator transitions. Taking into account the diurnal variation of $h_{max}, \Delta h$ does not significantly improve the model, since these changes can be compensated by changes in the f_oF2 parameter.

The use of the cosine of solar zenith angle $\Theta(t)$ and the small time delay ΔT allows us describing the GS dynamics during sunrise and sunset more accurately and including the geographic position of the radar into the model. The choice of normalization in (7) is made so that $\varepsilon(t)$ takes values in the range $[0,1]$ during the day. Therefore $\varepsilon(t)$ reaches its maximal value near noon and its minimal value near midnight. As a result the model for $f_oF2(t)$ (6) also reaches its maximal value $f_{oF2,max}$ near noon and its minimal value $f_{oF2,min}$ - near midnight.

When searching for optimal parameters of the model (3), the constant height of the maximum h_{mF2} and the half-thickness of the parabolic layer Δh were assumed to be 350 km and 100 km, respectively. The variations allowed in the model are the following:

$$\begin{cases} f_{oF2,max} \in [1, 33] MHz; \\ f_{oF2,min} \in [\frac{1}{16}, \frac{7}{16}] \cdot f_{oF2,max} MHz; \\ \beta \in [1, 5]; \\ \alpha \in [-1, 1]; \\ \Delta T \in [0, 3] hours \end{cases} \quad (8)$$

An important problem in approximating the experimental data is the fitting method. A feature of the GS signal is its asymmetric character (1): it has a shorter front at ranges below GS signal power maximum, and a longer rear at ranges above GS signal power maximum. Therefore, the distribution of errors in determining the GS signal can be asymmetric near the mean value. Because of this, the use of the standard least squares method, oriented to "white" symmetrical noise, can produce a regular error. The existence of ionospheric scattering and several propagation modes aggravates the situation even more and substantially increases the approximation errors.

To improve the accuracy of the approximation, a special fitting method has been developed to detect GS-signal smooth dynamics in the presence of signals not described by the GS model. The fitting method consists of three stages. At the first stage, the preliminary fitting of the model is made. This stage is required for preliminary rejection of ionospheric scattering and possible additional modes of propagation. At the second stage, we reject those signals, which differ significantly by range from the model. At the third stage, the final fitting of the model is made. During the first and third stages, a genetic algorithm is used (Simon, 2013), as a method of searching for an optimum, but with different input data and with different functionals of the optimum. At the second stage a kind of cluster analysis (Bailey, 1994) is used.

An illustration of the algorithm operation is shown in Fig.3A-F for 18/04/2016 experimental data. There is good correspondence between the model range and the regular dynamics of the power of the scattered signal, which indicates a generally good stability of the technique. Violet circles denote the points of the GS, extracted from the radar data and serve as input for the first algorithm stage. The blue crosses denote the points that passed the second stage (exclusion of ionospheric scattering). The black lines represent the model dynamics of the GS signal range calculated at the third stage. The line can be discontinuous due to changes of radar operational frequency or night propagation conditions. It can be seen from the figure that qualitatively the technique fits the GS radar range quite well.

Let us describe the fitting stages in detail.

The points participating in the first stage fitting were determined by the following condition:

$$R_{exp}(Bm, t) = \operatorname{argmax}_R(P(Bm, t, R) : GSFLAG(Bm, t, R) = true) \quad (9)$$

where Bm is the beam number, t is the time, $GSFLAG$ is the GS attribute at the given range, calculated by the standard FitACF algorithm (Ponomarenko & Waters, 2006). The selection rule (9) means that at each moment and on each beam a single point is found in which the power of the scattered signal is the maximal over all the signals defined as a GS at this moment and this beam. Thus, at each moment and for each beam, not more than a single point is selected, which is used later for fitting. A complete set of points participating in the fitting on a single beam is shown in Fig.3A-F by violet circles.

At the first stage, the fitting of the model (3,6,8) is made over these selected points (this corresponds to 24 hours of measurements at a single beam). In order to reduce the error in the presence of ionospheric scatter and additional modes, we used the following optimizing condition for the fitting:

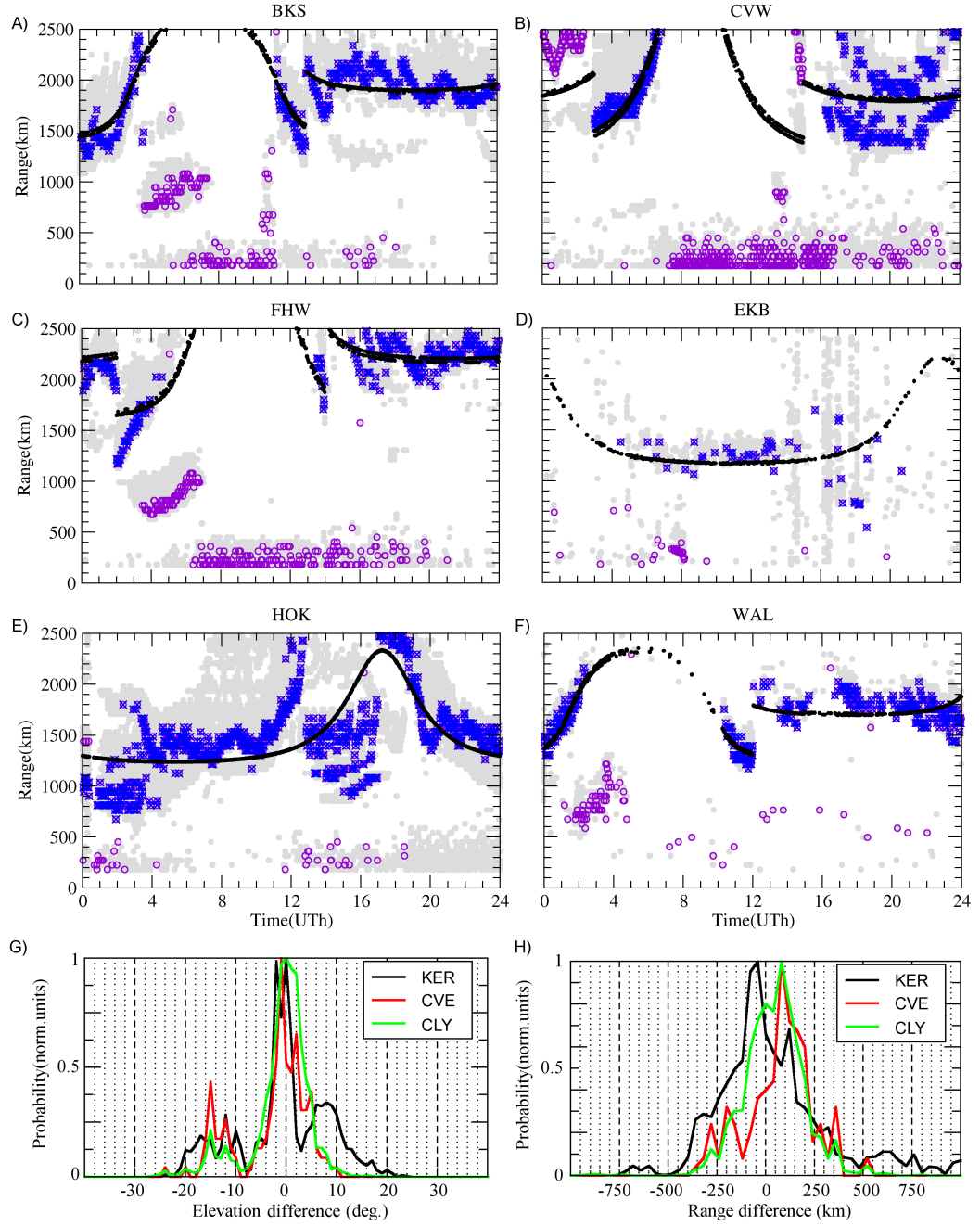


Figure 3: A-F) Illustration of the work of the fitting technique on various radars during 18/04/2016. Violet - non-GS data, detected at the second stage; blue - GS data, used for 3rd stage; black - GS distance, detected at 3rd stage. G) - the distribution of difference between model and measured GS elevation angles according to the KER, CVE and CLY radar data 18/04/2016. H) - the distribution of difference between model and measured GS range according to KER, CVE and CLY radar data 18/04/2016.

$$\Omega(Bm) = \sum_{i=0}^N W(\delta R_{exp,i}) = \max \quad (10)$$

where N is the total number of selected points (9) in the data involved in the fitting, and $W(\delta R_{exp,i})$ is the weight function. The maximization function (10) and the determination of the ionospheric parameters are carried out separately for each beam Bm . We do not require these model parameters to be close to each other on different beams. Our aim is to get smooth and physically reasonable radar distances and elevation angles. Their correctness will be discussed later.

The difference $\delta R_{exp,i}$ of the experimental range from the model range is defined as:

$$\delta R_{exp,i} = R_{model,i} - R_{exp,i} \quad (11)$$

Due to the asymmetric structure of GS signal over range, an asymmetric weight function W was chosen:

$$W(\delta R_{exp}) = \begin{cases} e^{-\frac{\delta R_{exp}}{200[km]}}; \delta R_{exp} \geq 0 \\ e^{\frac{\delta R_{exp}}{20[km]}}; \delta R_{exp} < 0 \end{cases} \quad (12)$$

This function W takes its maximal value when the experimental data coincide with the model data ($\delta R_{exp} = 0$), and falls to zero if they differ too much ($|\delta R_{exp}| \rightarrow \infty$).

The choice of characteristic scales of 20 and 200 km is related to the characteristic durations of the edges of the GS signal. It is obvious that using such a weight in white noise conditions give a biased estimate - the model curve passes on average not in the middle of the experimental points set, but closer to its lower boundary, approximately with the ratio 1:10. However, in this problem the result corresponds well to the physical meaning and structure of the GS signal: its maximal power position is shifted to smaller distance, so this should qualitatively compensate the 'non-whiteness' of the observed GS range variations. It should set the model of GS range closer to reality than the range calculated by the standard least-squares method. On the other hand, the use of such a weight function makes it possible to minimize the contribution of points substantially away from the model track (these are ionospheric scatter and other propagational modes) and to discard them from consideration during fitting.

As shown by qualitative analysis, the use of the weight function makes it possible to increase the stability of the technique in the presence of other modes and ionospheric scatter, and to carry out a model track near the lower boundary of the experimental GS data, which corresponds to the maximal energy of the GS signal.

The second stage of the algorithm is the rejection of ionospheric scattering and other propagation modes from the data. It is based on the cluster analysis technique, and close to the one used in (Ribeiro et al., 2011). All the points are put into range-time grid of values (100x100). Thus the normalized range and moment of each point are scaled to integer values [0,100]. For all the combinations of such points (i.e. pairs), an Euclidean distance is calculated, and the points are divided into a clusters based on the distances between them. Every point in a single cluster has a nearest neighbor point in the same cluster

at distance that does not exceed the doubled median distance calculated over the whole dataset. This allows us to separate the dataset into isolated clusters.

If the optimal model GS curve, calculated at the first stage, crosses a cluster at least at one point, the whole cluster is considered a GS signal. Otherwise the cluster is considered as not GS signal, and all the cluster points are excluded from subsequent consideration. The signals defined in the second stage as GS signals are shown by blue crosses in the Fig.3A-F, other signals are rejected at this stage and marked in the Fig.3A-F by violet circles.

In the third stage we believe that only F-layer GS signal points exist in the filtered data, and we can use the traditional least squares method to fit the model GS range function to the data:

$$\Omega(Bm) = \sum_{i=0}^M \delta R_{exp,i}^2 = \min \quad (13)$$

where M is the number of GS points remaining after the second stage. The fitting of the modelled GS range at the third stage is shown in the Fig.3A-F by the black line.

In Fig.3A-F one can also see conditions for which the algorithm does not work well. This happens when ionospheric scattering appears at distances that are close to the daytime GS distance (Fig.3E, 00-03UT, 12-17UT; Fig.3F, 15-19UT). Since X-ray solar flares effects are observed mostly during the day (Berngardt et al., 2018), the nighttime areas are not statistically important for this paper. So we do not pay attention to possible nighttime model range errors. A more critical problem is the case when the 1st and 2nd hop signals (Fig.3B, 17-24UT) are observed equally clearly and with nearly the same amplitude. So the model signal is forced to pass in the middle between these tracks. In this case, a significant regular error appears. Therefore, for a small amount of validated data, (Fig.3D), the algorithm can fail.

The model results have been compared with measurements made by the polar cap (CLY), sub-auroral (KER) and mid-latitude (CVE) radars on 18/04/2016. The root-mean-square error between the model elevation angle and the experimental measurements calculated from the interferometric data is $6 - 9^\circ$, with an average error of $1 - 3^\circ$ (Fig.3G). The root-mean-square error between the model GS range and the experimental measurements calculated for 18/04/2016 for these radars is 166-315 km, with an average error of 7-47 km (Fig.3H). The comparison shows that the technique can be used for processing polar cap, sub-auroral, and mid-latitude radar data.

In conclusion, in most cases, the algorithm works well enough to enable proper statistical conclusions. The smallness of the average range and elevation angle errors make it possible to use this technique for determining the model GS to carry out statistical studies on a large volume of experimental radar data.

Finally, to identify which hop produces most of the noise absorption, we analyzed the cases when the 1st hop and 2nd hop GS signal locations are at opposite sides of the solar terminator (i.e. in lit and unlit regions). We studied only cases when the noise absorption correlates well with X-rays at 1-8Å. The 2nd hop GS distance was estimated by doubling the first hop GS distance (4). This allows us to estimate geographical location of 2nd hop GS region. Since the absorption correlating with X-rays is mainly associated with the lit area (Berngardt et al., 2018), the studied cases allow us to statistically identify the

(lit) hop of most effective absorption. For the ≈ 400 cases found with the correlation coefficient $R > 0.6$ the probability of the absorption at the 1st hop is 78%. For the ≈ 70 cases found with $R > 0.9$ the probability of absorption at the 1st hop is 95.5%.

We made a similar comparison of the point above the radar and the point near the edge of the GS region. Our analysis has shown that the probability of absorption near GS region for $R > 0.8$ (over 15 cases) is 54%, for $R > 0.85$ (over 10 cases) is 75% , and for $R > 0.9$ (over 4 cases) is 100%.

Therefore, in most situations, the daytime noise absorption can be interpreted as absorption on the 1st hop, with the most probable location near the dead zone.

3 Dependence of the absorption on the sounding frequency

Using the model of the GS signal range described above, it is possible to automatically estimate the elevation angle of the incoming noise signal and, thereby, to transform the oblique absorption to the vertical absorption. Knowing the height of the absorbing region and the range to GS, it is possible to estimate the geographical position of the absorbing region.

Another important factor that needs to be taken into account is the frequency dependence of the absorption. Using it one can interpolate the absorption measured at the radar operating frequency to the absorption at a fixed frequency. At present, several variants of absorption frequency dependence are used in the analysis of experimental data and forecasting. The DRAP2 model (DRAP Documentation, 2010; Akmaev, R. A., 2010) and some nowcast PCA models (Rogers & Honary, 2015) use a frequency dependence given by $A[dB] = A_0 f^{-1.5}$, based on (Sauer & Wilkinson, 2008). A frequency dependence $A = A_0 f^{-1.24}$ is proposed in (Schumer, 2010). From the theory of propagation of radio waves, the frequency dependence for sufficiently high probing frequencies exceeding the collision frequency $2\pi f \gg \nu$ absorption should have the dependence $A = A_0 f^{-2}$ (Davies, 1969; Hunsucker & Hargreaves, 2002). Computational models like (Eccles, Hunsucker, Rice, & Sojka, 2005; Pederick & Cervera, 2014) use an ionospheric and a radio wave propagation model to calculate the absorption on each particular path and do not use an explicit frequency dependence.

To perform a comparative statistical analysis on a larger radar dataset, it is necessary to retrieve the experimental dependence of the absorption on the frequency of the radar. To determine this dependence, a correlation analysis of the absorption at various frequencies was carried out. We selected 'multi-frequency experiments', that is, experiments for which, during 6 minutes, a certain radar simultaneously operated at least on 2 frequencies, separated by at least 10%, at the same azimuth. After selecting these experiments we built regression coefficients between the noise levels at different frequencies for each 'multi-frequency experiment' , taking into account the possibility of different background noise levels and their various (linear) time dependencies. Thus, the regression coefficient A_0 for each 'multi-frequency experiment' was determined as the value minimizing the root-mean-square deviation of noise attenuation

$P_1(t), P_2(t)$ at frequencies f_1, f_2 respectively. In other words, A_0 is defined as the solution to the problem:

$$\Omega = \int_{T_{flare}-1h}^{T_{flare}+2h} (P_1(t)[dB] - \{A_0 P_2(t)[dB] + A_1 + A_2 t\})^2 dt = \min \quad (14)$$

The integration was made over the regions $P_1(t) < 0.9 \cdot \max(P_1), P_2(t) < 0.9 \cdot \max(P_2)$ to exclude noise saturation effects from consideration. To increase the validity of the retrieved data, we analyzed only the cases where the correlation coefficient between the noise attenuation and the variations of the intensity of solar radiation in the 1-8 Å band exceeded 0.4, which indicates a statistically significant absorption effect (Berngardt et al., 2018). As a result, we obtained a statistical distribution of the exponent of the power-law dependence of the absorption on the frequency

$$A[dB] \sim f^{-\alpha} \quad (15)$$

by calculating the ratio for every experiment:

$$\alpha_i = \frac{\log(A_{0,i})}{\log(f_{1,i}/f_{2,i})} \quad (16)$$

where $f_{2,i}, f_{1,i}$ are the frequencies of noise observation simultaneously on the same beam at the same radar, and $A_{0,i}$ is the coefficient of regression between the absorption and X-ray flare dynamics at different sounding frequencies; i is the experiment number.

Fig.4A shows the parameters of statistical distribution of α calculated over 'multi-frequency experiments' for relatively high frequency difference ($f_1/f_2 \in [1.2, 1.3]; f_1/f_2 \in [1.3, 1.5]; f_1/f_2 \in [1.5, 1.6]$) and absorption for correlating ($|R| > 0.4$) with 1-8 Å solar radiation. To improve the estimates, we selected only experiments with small carrier frequency variations $\delta f_1, \delta f_2$ during flare observations ($|\delta f_1|, |\delta f_2| < 150 kHz$) around the average sounding frequencies (f_1, f_2). In other words, we investigated multi-frequency experiments with a large enough difference between two frequencies, that is, we required

$$|f_1 - f_2| > 3 \cdot (|\delta f_1| + |\delta f_2|) \quad (17)$$

This final distribution corresponds to 1662 individual experiments at 18 different radars (BKS, BPK, CLY, DCE, EKB, GBR, HKW, HOK, INV, KAP, KOD, KSR, MCM, PGR, RKN, SAS, TIG, WAL). It can be seen from Figure 4 that the distribution of α has an average around 1.6 (for $f_1/f_2 > 1.3$) and RMS can reach about 0.3 (at $f_1/f_2 > 1.5$). The statistics indicate that the dependence of the absorption on the frequency in the range 8-20 MHz can be described more stably by the empirical dependence $A[dB] \sim f^{-1.6}$, which is close to $\alpha = 1.5$, used in the conventional absorption forecast model DRAP2 (DRAP Documentation, 2010; Akmaev, R. A., 2010). Therefore, we will use the empirically found value $\alpha = 1.6 \pm 0.3$ in the following work.

4 Correlation of absorption dynamics with solar radiation of different wavelengths

The next important issue arising in the investigation of noise data by coherent radars is the interpretation of the detailed temporal dynamics of the noise absorption. As shown in (Berngardt et al., 2018) and seen in fig.1A-C, the front of noise absorption at the radar correlates well with the shape of the X-ray flare according to GOES/XRS 1-8Å. The rear is substantially delayed with respect to the X-ray 1-8Å flare. As the preliminary analysis showed, this is a relatively regular occurrence for the data from 2013 to 2017. Since the absorption from the rear is delayed for tens of minutes, it cannot be explained only in terms of recombination in the ionized region.

One possible explanation for the delay in the rear is the contribution to ionospheric absorption of regions higher than the D layer, ionized by solar radiation lines other than the X-ray 1-8 Å. It is known that the lower part of the ionosphere (layers D- and E-) is ionized by wavelengths <100 Å (Banks & Kockarts, 1973) as well as by Lyman- α line (about 1200Å). Most often, researchers analyze the association of absorption with X-ray radiation 1-8 Å only, measured by GOES/XRS and associated with the ionization of the D-layer (Rogers & Honary, 2015; Warrington et al., 2016), see fig.1D. However, the absorption is important not only in the D-layer but also in the E-layer, the ionization of which is caused by other components of the solar radiation. In particular, soft X-ray 10-50 Å radiation is taken into account in modern D-layer ionization models (Eccles et al., 2005) (where it is taken into account using a solar spectrum model). The combined effect of increasing absorption in the E-layer and a slight refraction extending the path length in the absorbing layer leads to the need to take into account the ionization of the E-layer.

To analyze the correlation of the noise attenuation with various solar radiation lines, we carried out a joint analysis of the absorption during the 80 flares of 2013-2017 and data from varied instruments, namely: GOES/XRS (Hanser & Sellers, 1996; Machol & Viereck, 2016), GOES/EUVS (Machol, Viereck, & Jones, 2016), SDO/AIA (Lemen et al., 2012), PROBA2/LYRA (Hochedez et al., 2006; Dominique et al., 2013), SOHO/SEM (Didkovsky et al., 2006), SDO/EVE(ESP) (Didkovsky, Judge, Wieman, Woods, & Jones, 2012). These instruments provide direct and regular observations of solar radiation in the wavelength range 1-2500Å during the period under study (see Table 2 for details). It is well known that at different wavelengths the solar radiation dynamics during flares is different (Donnelly, 1976). This allows us to find the solar radiation lines that most strongly influence the dynamics of the noise variations at the coherent radars.

To determine the effective ionization lines, we calculate the following probability:

$$P(\Lambda) = P(R(P(t), I_{\Lambda}(t)) \geq R(P(t), I_{1-8\text{Å}}(t)) | R(P(t), I_{1-8\text{Å}}(t)) \geq 0.4) \quad (18)$$

In this expression, $P(\Lambda)$ is the probability that the correlation coefficient $R(P(t), I_{\Lambda}(t))$ of the observed absorption $P(t)$ with the intensity $I_{\Lambda}(t)$ of a given solar radiation line Λ during the X-ray flare period will not be lower than the correlation coefficient $R(P(t), I_{1-8\text{Å}}(t))$ of the observed absorption $P(t)$ with the intensity

$I_{1-8\text{\AA}}(t)$ of GOES/XRS 1-8 \AA line. The calculations are carried out only for cases during which the correlation coefficient between absorption and GOES/XRS solar radiation is greater than 0.4.

It should be noted that if the distribution of values of the correlation coefficients are similar and independent for different wavelengths of solar radiation, then $P(\Lambda)$ should not exceed 0.5. Exceeding this level indicates a line of solar radiation to be a controlling factor for the attenuation of the noise. Figure 4B shows the results of this analysis based on the processing of over 11977 individual observations.

One can see from Figure 4B that very often (in 62 to 68% of the cases) $P(\Lambda)$ exceeds 0.5 for Λ in the ranges SDO/AIA 94 \AA , SDO/EVE 1-70 \AA , 300-340 \AA , SDO/AIA 304,335 \AA , SOHO/SEM 1-500 \AA . This indicates the need to take these solar radiation lines into account when interpolating the HF noise attenuation. All these lines are absorbed below 150 km (Tobiska, Bouwer, & Bowman, 2008, fig.2). They are therefore sources of ionization in the lower part of the ionosphere and are contributing to the radio noise absorption observed in the experiment.

Let us demonstrate the potential of using the linear combination of six lines from these spectral ranges (1-8 \AA , 94 \AA , 304 \AA , 335 \AA , 1-70 \AA , 1-500 \AA) instead of just single 1-8 \AA GOES/XRS line. Let us assume that ionization is produced by different lines independently, the contributions of each line to ionization are positive, and are retrievable. To search for the amplitude of these contributions, we used the non-negative least-squares method (Lawson & Hanson, 1995). It provides an iterative search for the best approximation of experimental noise attenuation $P_{att}(t)$ by a linear combination of solar radiation dynamics at different wavelengths ($P_{1-8\text{\AA}}(t)$, $P_{94\text{\AA}}(t)$, $P_{304\text{\AA}}(t)$, $P_{335\text{\AA}}(t)$, $P_{1-70\text{\AA}}(t)$, $P_{1-500\text{\AA}}(t)$) with unknown nonnegative weighting multipliers. In addition we also take into account slow background noise dynamics by adding a linear dependence $C_0 + C_1 t$ into the regression.

Finally, we search for parameters $C_{0..7}$ that solve the problem:

$$\int_{T_{flare}-1h}^{T_{flare}+2h} (P_{att}(t) - C_0 - C_1 t - C_2 P_{1-8\text{\AA}}(t) - C_3 P_{94\text{\AA}}(t) - C_4 P_{304\text{\AA}}(t) \quad (19)$$

$$- C_5 P_{335\text{\AA}}(t) - C_6 P_{1-70\text{\AA}}(t) - C_7 P_{1-500\text{\AA}}(t))^2 dt = \min \quad (20)$$

under the limitation that $C_2, C_3, C_4, C_5, C_6, C_7$ be all positive.

Examples of approximations and statistical results are shown in Fig.4C-F. It can be seen that the sum of four lines (dot-dashed green line) approximates the experimental data much better than just a single GOES/XRS (dotted black line) solar radiation line. Fig.4C shows the distribution of the correlation coefficients when the experimental data are approximated by linear combinations of the lines 1-8 \AA , 94 \AA , 304 \AA , 335 \AA , 1-70 \AA , and 1-500 \AA . The figure shows that the combination of the lines 1-8 \AA and 94 \AA (solid black line) fits the experimental data no worse than the combination of all six lines (dot-dashed green line), and significantly better than the single line 1-8 \AA (dotted black line). This allows us to use a combination of the two lines 1-8 \AA and 94 \AA as parameters of the noise attenuation model during X-ray solar flares at these radars.

In this paper we analyze only X-ray flares, and the level of Lyman- α line is comparatively weak. Therefore the well-known dependence of the D-layer

ionization with Lyman- α is not detected (see Fig.4B).

Lines 10-100Å are usually absorbed at heights of the order of and below 100 km (Banks & Kockarts, 1973, fig.1.7, par.6.3.). This indicates a significant contribution of the lower part of the E-layer to the noise absorption observed by the radars.

The median value of the correlation coefficient of the noise attenuation with 1-8Å is 0.62, with the combination of 1-8Å + 94Å lines is 0.76, and with the combination of all 6 lines is 0.73.

Thus, taking into account the line 94Å leads to an increase in the median correlation coefficient from 0.62 to 0.76, while adding other lines does not significantly increase the correlation. This allows us concluding that use of the 1-8Å and 94Å solar radiation lines as a proxy of the noise attenuation profile potentially allows a more accurate approximation of the temporal dynamics of the experimentally observed noise attenuation, and as a result, of the temporal dynamics of the absorption of the HF radio signals in the lower part of the ionosphere. Fig.4D-L shows the attenuation of HF noise dynamics when it is approximated only by GOES/XRS 1-8Å (green dashed line) and by a combination of GOES/XRS 1-8Å and SDO/AIA 94Å solar radiation (red line). The approximations are shown for several radars during several flares. It can be seen from the figure that taking into account intensity of the SDO/AIA 94Å line significantly improve the accuracy of fitting the noise attenuation dynamics. Therefore it is necessary to take into account not only the D-layer, but also the E-layer of the ionosphere for the interpretation of the noise absorption during X-ray solar flares. This corresponds well with the results obtained by (Eccles et al., 2005).

5 Diagnostics of global absorption effects

Taking into account all of the above, it is possible to build an automatic system suitable for global analysis of ionospheric absorption of HF radio waves over the area covered by radar field-of-views. The algorithm for constructing the automatic absorption analysis system consists of the following stages.

At the first stage, the GS signal range curve is determined from the daily behavior of the GS signal. We model the ionosphere as a parabolic layer of known half-thickness Δh and height h_{mF2} , but of unknown amplitude $f_{oF2}(t)$ and dynamics. The temporal dynamics of $f_{oF2}(t)$ is approximated by the nonlinear parametric function (6), and its parameters are calculated from experimental data via a fitting procedure.

Using this GS signal range curve, the elevation angle of the received GS signal is estimated as a function of time. The location of the region making the main contribution to the absorption of the radio noise is found simultaneously. Its calculation is based on the Breit-Tuве principle (Davies, 1969) and on the assumption that the signal is reflected at the virtual height h_{mF2} . Such a calculation is carried out separately for each radar, for each beam. The algorithm for constructing the dynamics of GS range and the elevation angle is given above (3,5).

At the second stage, the noise absorption level $\tilde{P}_{vert,10MHz}(t, \phi(t), \lambda(t))$ is estimated for the vertical radio wave propagation in the absorbing layer at a frequency of 10MHz for each beam of the radar, at a geographical point $(\phi(t), \lambda(t))$

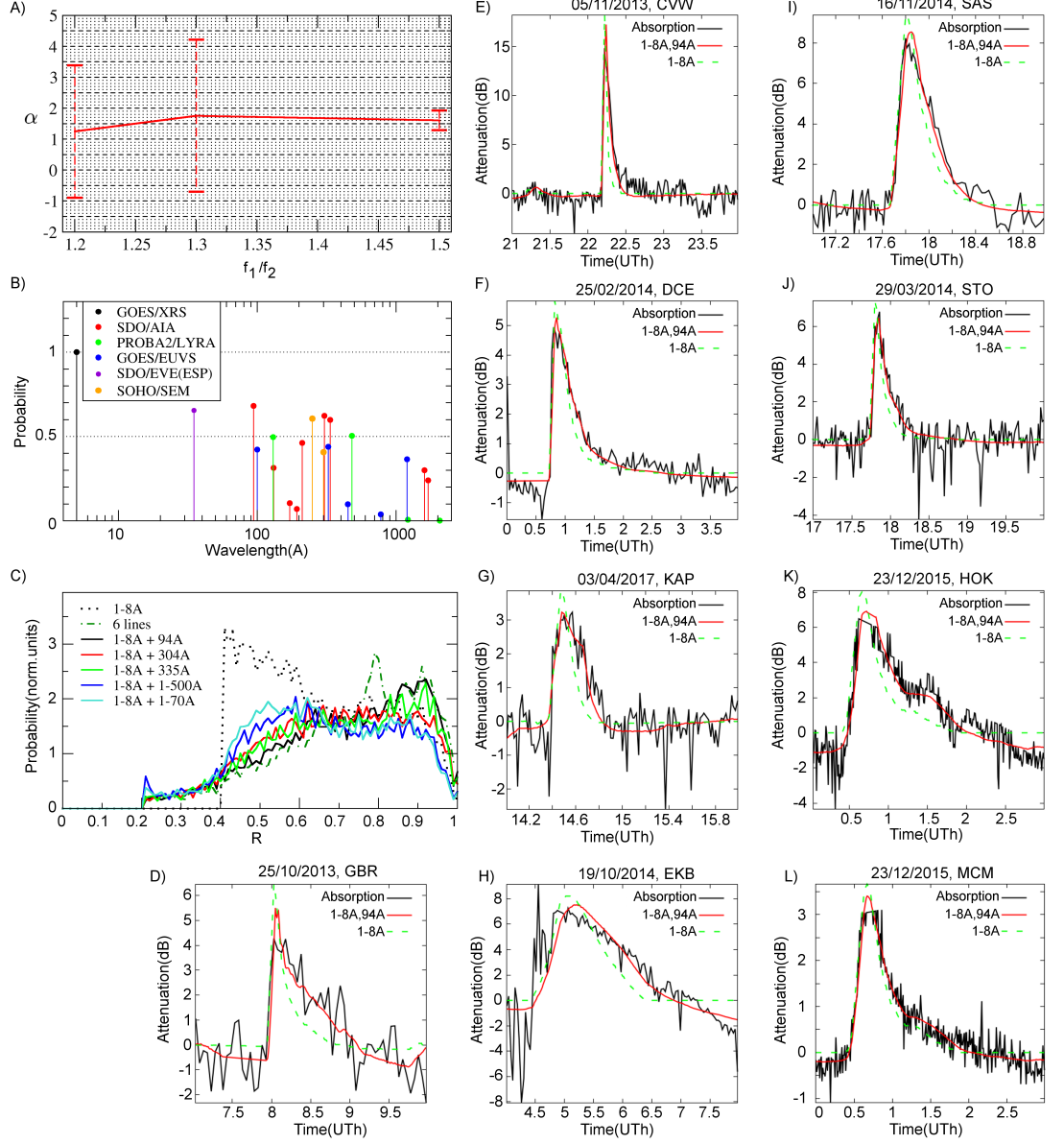


Figure 4: A) Average and RMS of the power-law (15) coefficient α of the absorption frequency dependence as a function of relation of frequencies during multi-frequency experiments; B) The probability $P(\lambda)$ (18) over all the flares and the radars; C) Distribution of correlation coefficients for various approximations of the noise absorption experimental data; D-L) are examples of fitting the attenuation of HF noise by different combinations of solar spectrum lines (at different radars during different X-ray flares).

corresponding to the position of the effective absorbing region. It is calculated from the noise variations $\tilde{P}(t)$ detected by the radar, taking into account the elevation angle Θ_{model} of the radio signal propagation in the absorbing layer, which was calculated at the first stage. The absorption corresponds to the geographic coordinates $(\phi(t), \lambda(t))$, also calculated in the first stage, and set to the point which is farthest away from the radar (the trajectory crosses D-layer at two points). The observed dependence of absorption on frequency $f(t)$ is interpolated to 10MHz frequency using our retrieved median frequency dependence. The resulting expression for the vertical absorption is:

$$\tilde{P}_{vert,10MHz}(t, \phi(t), \lambda(t)) = \tilde{P}(t) \sin(\Theta_{model}(t)) \left(\frac{f(t)}{f_0} \right)^{1.6} \quad (21)$$

where $f_0 = 10\text{MHz}$, and $f(t)$ is the radar sounding frequency.

Fig.5A-H shows the absorption dynamics over the radars field-of-views during the 07/01/2014 solar flare based on the proposed algorithm. One can see the global-scale absorption effect between 18:18 UT and 19:12 UT that corresponds to the solar X-ray flare. Each radar produces several measurement points, corresponding to the number of beams, one beam - one measurement point.

So the spatial resolution and resolved areas depend on radiowave propagation characteristics and could vary from flare to flare. For future practical purposes one can fit the obtained absorption measurements over space by a smoothing function or join them with regular riometric measurements.

One of the ways to smooth the obtained data is through their accumulation over latitude or longitude. It allows us to more clearly distinguish the temporal dynamics of absorption and to reveal its average latitudinal or longitudinal dependencies.

Fig.5I shows the dynamics of median absorption as a function of latitude during this event. The median was calculated over 3 geographical degrees. Fig.5J shows the dynamics of median absorption as a function of longitude during this event. The median was calculated over 3 geographical degrees. For comparison solar radiation at $1-8\text{\AA}$ and 94\AA is shown in Fig.5K. It can be seen from the figure that the proposed method makes it possible to investigate the spatio-temporal dynamics of absorption over a significant part of the Earth's surface.

A joint analysis of Fig.5A-J allows, for example, to distinguish absorption regions in the lit area that correlate well with the flare (green regions) from the effects in the unlit area that can not be correctly interpreted with the approach taken in this paper. The system that we have constructed can be used for studies of spatio-temporal features of daytime absorption both as a separate network and with other instruments and techniques.

6 Conclusion

In the present work, a joint analysis was carried out of the data of 35 HF over-the-horizon radars (34 SuperDARN radars and the EKB ISTP SB RAS radar) during 80 solar flares of 2013-2017. The analysis shows the following features of the absorption of 8-20MHz radio noise.

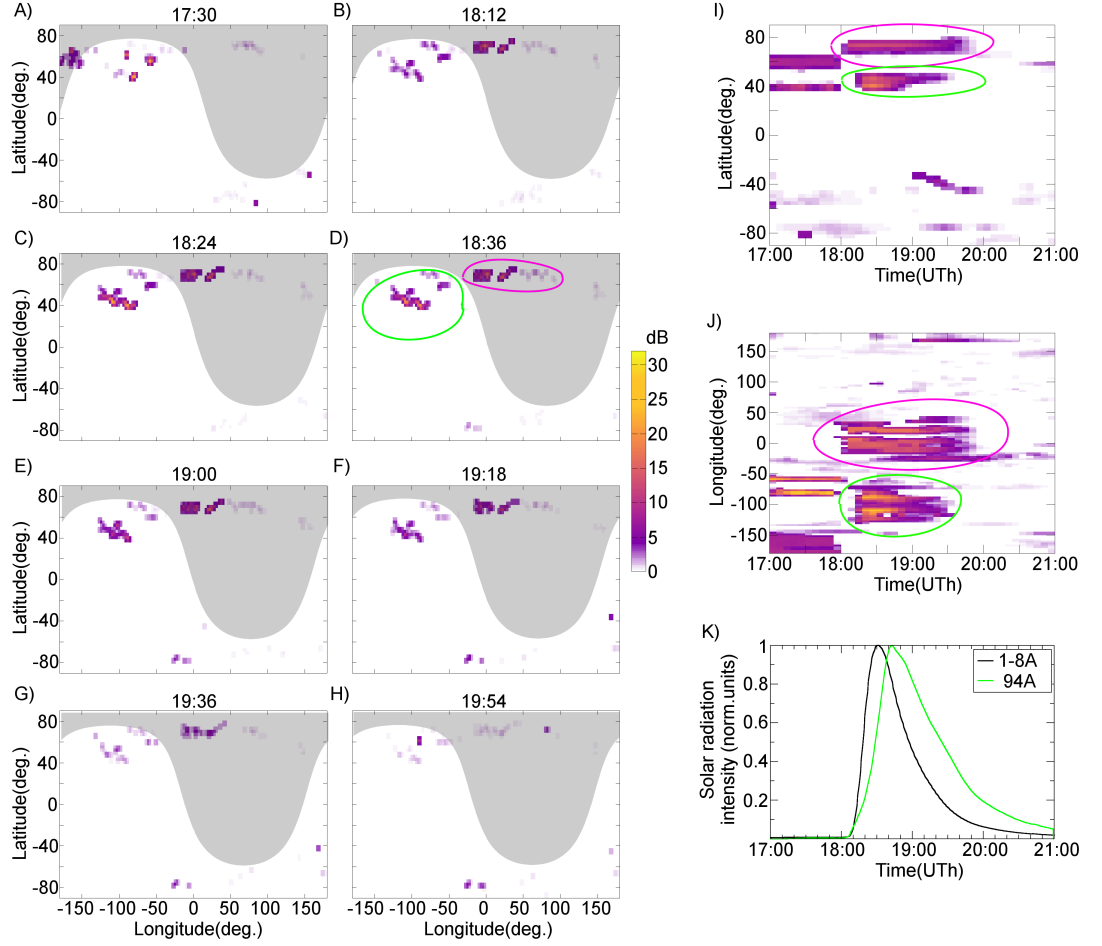


Figure 5: A-H) - vertical absorption dynamics at 10MHz during solar X-ray flare X1.2 07/01/2014 according to the radar network and model (21). Grey region marks unlit area at 100km height. I) - latitude absorption dynamics during the flare, median over all the longitudes; J) - longitude absorption dynamics during the flare, median over all the latitudes; K) the intensity of solar radiation from the data of GOES/XRS 1-8Å and SDO/AIA 94Å. Color scale is the same for the figures A-J). Green and violet regions mark effects in lit and unlit conditions.

The position of an effective noise source on the ground and the error in determining its location can be determined by the position of spatial focusing at the boundary of the dead zone and the form of this focusing (ground scatter signal). This allows using the GS signal to estimate the position of the region that makes the main contribution to the observed absorption of the HF radio noise at a particular radar frequency.

The analysis of the correlation between different solar radiation lines and HF noise dynamics has shown that the temporal variation of the absorption is well described by a linear combination of the solar radiation intensity at the wavelengths 1-8Å measured by GOES/XRS and at the wavelength of 94Å measured by SDO/AIA. This allows us to conclude that the main absorption is caused by ionospheric D and E layers. The assumption we used in our paper about a linear superposition of the contributions of each solar line to absorption is relatively rough. To solve more accurately for the reconstruction of the electron density profile from the experimentally observed noise absorption and from the solar spectrum, it is necessary to take into account the processes of ionization by the various radiation components and corresponding delays more correctly, for example, following the approach of (Eccles et al., 2005).

The frequency dependence of the HF absorption is determined by the median dependence $A[dB] \sim f^{-1.6 \pm 0.3}$.

A model and algorithms are constructed (21), that provides automatic radar estimates of vertical daytime absorption at 10 MHz. Using these model algorithms, it is possible to make statistical analysis and case-studies of the spatio-temporal dynamics of the absorption of HF radio waves globally, within the coverage area of radar field-of-views. Each radar produces several measurement points, corresponding to the number of beams, one beam - one measurement point. So the spatial resolution and resolved areas depend on radiowave propagation characteristics and will vary from flare to flare.

One important problem with the algorithm constructed here is the determination of the geographical location of the absorption region during the day. This location depends on whether the most intense 1-hop absorption is located near the radar or near the GS distance of the first hop. A similar problem arises with the URSI A1 method. For future applications, one might want to fit the retrieved absorption measurements through the use of a smoothing function over space. However, at night or near the terminator, this algorithm should not be used.

Another problem of the algorithm is the impossibility of taking into account irregular variations in the background ionosphere. This is important for a more correct estimation of ray trajectory and, as result, for more accurate estimation of the vertical absorption from the experimental data for specific observations. The use of calibrated experimental measurements of the ray elevation angles of GS signals and new techniques for identifying GS signals from radar data should help to solve this problem in the future.

Acknowledgments

The data of the SuperDARN radars were obtained using the DaViT (<https://github.com/vtsuperdarn/davitpy>), the EKB ISTP SB RAS radar data are the property of the ISTP SB RAS, contact Oleg Bergardt (berng@iszf.irk.ru). The authors

are grateful to all the developers of the DaViT system, in particular K.Sterne, N.Frissel, S. de Larquier and A.J.Ribeiro, as well as to all the organizations supporting the radars operation. O.B. is grateful to X.Shi (Virginia Tech) for help in using DaViT. In the paper we used the data of EKB ISTP SB RAS, operating under financial support of FSR Program II.12.2. The authors acknowledge the use of SuperDARN data. SuperDARN is a collection of radars funded by the national scientific funding agencies of Australia, Canada, China, France, Italy, Japan, Norway, South Africa, United Kingdom and United States of America. The SuperDARN Kerguelen radar is operated by IRAP (CNRS and Toulouse University) and is funded by IPEV and CNRS through INSU and PNST programs. The Dome C East radar was installed in the framework of a French-Italian collaboration and is operated by INAF-IAPS with the support of CNR and PNRA. The SuperDARN SENSU Syowa East and South radars are the property of National Institute of Polar Research (NIPR), this study is a part of the Science Program of Japanese Antarctic Research Expedition (JARE) and is supported by NIPR under Ministry of Education, Culture, Sports, Science and technology (MEXT), Japan. The SuperDARN Canada radar operations (SAS, PGR, INV, RKN, CLY) are supported by the Canada Foundation for Innovation, the Canadian Space Agency, and the Province of Saskatchewan. The authors thank SuperDARN Canada for providing the data from the two-frequency operating modes.

The authors are grateful to Altyntsev A.T., Tashchilin A.V., Kashapova L.K. (ISTP SB RAS) for useful discussions. The authors are grateful to NOAA for GOES/XRS and GOES/EUVS data (available at <https://satdat.ngdc.noaa.gov/sem/goes/data/>), to NASA/SDO and to the AIA and EVE teams for SDO/AIA and SDO/EVE data (available at <https://sdo.gsfc.nasa.gov/data/>, http://lasp.colorado.edu/eve/data_access/service/file_download/, <http://suntoday.lmsal.com/sun-today/>), to Royal Observatory of Belgium for PROBA2/LYRA data (available at <http://proba2.oma.be/lyra/data/bsd/>) used for analysis. The authors are grateful to The University of Southern California Space Sciences Center for using SOHO/SEM data, available at <https://dornsifecms.usc.edu/space-sciences-center/download-sem-data/>). Solar Heliospheric Observatory (SOHO) is a joint mission project of United States National Aeronautics and Space Administration (NASA) and European Space Agency (ESA). LYRA is a project of the Centre Spatial de Liege, the Physikalisch-Meteorologisches Observatorium Davos and the Royal Observatory of Belgium funded by the Belgian Federal Science Policy Office (BELSPO) and by the Swiss Bundesamt für Bildung und Wissenschaft. A.S.Y. is supported by Japan Society for the Promotion of Science (JSPS), "Grant-in-Aid for Scientific Research (B)" (Grant Number: 25287129). J.M.R. acknowledges the support of NSF through award AGS-1341918. O.I.B. is supported by RFBR grant #18-05-00539a.

References

- Akmaev, R. A. (2010). *DRAP Model Validation: I.Scientific Report*. Retrieved from <https://www.ngdc.noaa.gov/stp/drap/DRAP-V-Report1.pdf>
- Bailey, K. (1994). *Typologies and Taxonomies: An Introduction to Classification Techniques* (No. 102). SAGE Publications.

Table 1: The radars participating in the study

Code	Geogr.coord.	Full radar name	Owner
ADE	51.9N,176.6W	Adak Island East SuperDARN	University of Alaska, Fairbanks, USA
ADW	51.9N,176.6W	Adak Island West SuperDARN	University of Alaska, Fairbanks, USA
BKS	37.1N,77.9W	Blackstone SuperDARN	Virginia Tech, USA
BPK	34.6S, 138.5W	Buckland Park SuperDARN	La Trobe University, Australia
CLY	70.5N,68.5W	Clyde River SuperDARN	University of Saskatchewan, Canada
CVE	43.3N,120.4W	Christmas Valley East SuperDARN	Dartmouth College, USA
CVW	43.3N,120.4W	Christmas Valley West SuperDARN	Dartmouth College, USA
DCE	75.1S,123.3E	Dome C East SuperDARN	INAF-IAPS/CNR/PNRA, Italy
EKB	56.5N,58.5E	Ekaterinburg ISTP SB RAS	ISTP SB RAS, Russia
FHE	38.9N, 99.4W	Fort Hays East SuperDARN	Virginia Tech, USA
FHW	38.9N, 99.4W	Fort Hays West SuperDARN	Virginia Tech, USA
GBR	53.3N,60.5W	Goose Bay SuperDARN	Virginia Tech, USA
HAL	75.5S, 75.5W	Halley SuperDARN	British Antarctic Survey, UK
HAN	62.3N,26.6E	Hankasalmi SuperDARN	University of Leicester, UK
HKW	43.5N,143.6E	Hokkaido West SuperDARN	Nagoya University, Japan
HOK	43.5N,143.6E	Hokkaido East SuperDARN	Nagoya University, Japan
INV	68.4N,133.8W	Inuvik SuperDARN	University of Saskatchewan, Canada
KAP	49.4N,82.3W	Kapuskasing SuperDARN	Virginia Tech, USA
KER	49.2S, 70.1E	Kerguelen SuperDARN	IRAP/CNRS/IPEV, France
KOD	57.6N,152.2W	Kodiak SuperDARN	University of Alaska, Fairbanks, USA
KSR	58.7N,156.6W	King Salmon SuperDARN	National Institute of Information and Communications Technology, Japan
MCM	77.9S,166.7E	McMurdo SuperDARN	University of Alaska, Fairbanks, USA
PGR	54.0N,122.6W	Prince George SuperDARN	University of Saskatchewan, Canada
PYK	63.7N,20.5W	Pykkvibaer SuperDARN	University of Leicester, UK
RKN	62.8N,93.1W	Rankin Inlet SuperDARN	University of Saskatchewan, Canada
SAN	71.7S, 2.9W	SANAE SuperDARN	South African National Space Agency, South Africa
SAS	52.2N,106.5W	Saskatoon SuperDARN	University of Saskatchewan, Canada
SPS	-90.0S,118.3W	South Pole Station SuperDARN	University of Alaska, Fairbanks, USA
STO	63.9N,21.0W	Stokkseyri SuperDARN	Lancaster University, UK
SYE	69.0S, 39.6E	Syowa East SuperDARN	National Institute of Polar Research, Japan
SYS	69.0S, 39.6E	Syowa South SuperDARN	National Institute of Polar Research, Japan
TIG	43.4S, 147.2E	Tiger SuperDARN	La Trobe University, Australia
UNW	46.5S, 168.4E	Unwin SuperDARN	La Trobe University, Australia
WAL	37.9N,75.5W	Wallops ²⁴ Island SuperDARN	JHU Applied Physics Laboratory, USA
ZHO	69.4S,76.4E	Zhongshan SuperDARN	Polar Research Institute of China

Table 2: Spectral bands of solar instruments used in the paper and their reference average wavelength used in the paper

Satellite/Instrument	Spectral band	Reference wavelength (\AA)
GOES/XRS	1-8 \AA	5
GOES/EUVA	50-150 \AA	100
GOES/EUVB	250-400 \AA	325
GOES/EUVC	200-700 \AA	450
GOES/EUVD	200-850 \AA	525
GOES/EUVE	1150-1250 \AA	1200
SDO/AIA	94 \AA	94
SDO/AIA	131 \AA	131
SDO/AIA	171 \AA	171
SDO/AIA	193 \AA	193
SDO/AIA	211 \AA	211
SDO/AIA	304 \AA	304
SDO/AIA	335 \AA	335
SDO/AIA	1600 \AA	1600
SDO/AIA	1700 \AA	1700
PROBA2/LYRA (channel 1)	1200-1230 \AA	1215
PROBA2/LYRA (channel 2)	1900-2220 \AA	2060
PROBA2/LYRA (channel 3)	<50 \AA + 170-800 \AA	435
PROBA2/LYRA (channel 4)	<20 \AA + 60-200 \AA	130
SOHO/SEM (channel 2)	1-500 \AA	249
SOHO/SEM (channels 1+3)	260-340 \AA	300
SDO/EVE (ESP)	1-70 \AA	35

- Baker, J., Greenwald, R., Ruohoniemi, J., Oksavik, K., Gjerloev, J. W., Paxton, L. J., & Hairston, M. (2007). Observations of ionospheric convection from the Wallops SuperDARN radar at middle latitudes. *Journal of Geophysical Research (Space Physics)*, 112, A01303. doi: 10.1029/2006ja011982
- Baker, K. B., Greenwald, R., Villian, J. P., & Wing, S. (1988). *Spectral Characteristics of High Frequency (HF) Backscatter for High Latitude Ionospheric Irregularities: Preliminary Analysis of Statistical Properties* (Tech. Rep. No. ADA202998). Johns Hopkins Univ Laurel Md Applied Physics Lab.
- Banks, P., & Kockarts, G. (1973). *Aeronomy* (Vol. A). Academic Press, New York and London.
- Barthes, L., Andre, D., Cerisier, J. C., & Villain, J.-P. (1998). Separation of multiple echoes using a high-resolution spectral analysis for SuperDARN HF radars. *Radio Science*, 33(4), 1005–1017. doi: 10.1029/98rs00714
- Berngardt, O. I., Ruohoniemi, J. M., Nishitani, N., Shepherd, S. G., Bristow, W. A., & Miller, E. S. (2018). Attenuation of decameter wavelength sky noise during x-ray solar flares in 2013–2017 based on the observations of midlatitude HF radars. *Journal of Atmospheric and Solar-Terrestrial Physics*, 173, 1 - 13. doi: 10.1016/j.jastp.2018.03.022
- Berngardt, O. I., Zolotukhina, N. A., & Oinats, A. V. (2015). Observations of field-aligned ionospheric irregularities during quiet and disturbed conditions with EKB radar: first results. *Earth, Planets and Space*, 67(1), 143. doi: 10.1186/s40623-015-0302-3
- Bilitza, D., Altadill, D., Truhlik, V., Shubin, V., Galkin, I. A., Reinisch, B. W., & Huang, X. (2017). International Reference Ionosphere 2016: from ionospheric climate to real-time weather predictions. *Space Weather*, 418–429. (2016SW001593) doi: 10.1002/2016sw001593
- Blagoveshchenskii, D. V., Maltseva, O. A., Anishin, M. M., Rogov, D. D., & Sergeeva, M. A. (2015). Modeling of HF propagation at high latitudes on the basis of IRI. *Advances in Space Research*, 57(3), 821–834. doi: 10.1016/j.asr.2015.11.029
- Blanchard, G. T., Sundeen, S., & Baker, K. B. (2009). Probabilistic identification of high-frequency radar backscatter from the ground and ionosphere based on spectral characteristics. *Radio Science*, 44(5), RS5012. doi: 10.1029/2009rs004141
- Bland, E. C., Heino, E., Kosch, M. J., & Partamies, N. (2018). SuperDARN radar-derived HF radio attenuation during the September 2017 solar proton events. *Space Weather*. doi: 10.1029/2018sw001916
- Bliokh, P. V., Galushko, V. G., Minakov, A. A., & Yampolski, Y. M. (1988). Field interference structure fluctuations near the boundary of the skip zone. *Radiophysics and Quantum Electronics*, 31(6), 480–487. doi: 10.1007/bf01044650
- Chakraborty, S., Ruohoniemi, J. M., Baker, J. B. H., & Nishitani, N. (2018). Characterization of Short-Wave Fadeout Seen in Daytime SuperDARN Ground Scatter Observations. *Radio Science*, 53(4), 472–484. doi: 10.1002/2017RS006488
- Chernov, Y. A. (1971). *Backward-oblique sounding of the ionosphere(in russian)*. Moscow,Svyaz.
- Chisham, G. (2018). Calibrating SuperDARN Interferometers Using Meteor Backscatter. *Radio Science*, 53(6), 761–774. doi: 10.1029/2017RS006492

- Chisham, G., Lester, M., Milan, S., Freeman, M., Bristow, W., McWilliams, K., ... Walker, A. (2007). A decade of the Super Dual Auroral Radar Network (SuperDARN): scientific achievements, new techniques and future directions. *Surveys in Geophysics*(28), 33-109. doi: 10.1007/s10712-007-9017-8
- Davies, K. (1969). *Ionospheric radio waves*. Blaisdell Pub. Co.
- Detrick, D. L., & Rosenberg, T. J. (1990). A phased-array radiowave imager for studies of cosmic noise absorption. *Radio Science*, 25(4), 325-338. doi: 10.1029/RS025i004p00325
- Didkovsky, L. V., Judge, D., Wieman, S., Woods, T., & Jones, A. (2012). EUV SpectroPhotometer (ESP) in Extreme Ultraviolet Variability Experiment (EVE): Algorithms and Calibrations. *Solar Physics*, 275(1), 179-205. doi: 10.1007/s11207-009-9485-8
- Didkovsky, L. V., Judge, D. L., Jones, A. R., Wieman, S., Tsurutani, B. T., & McMullin, D. (2006). Correction of SOHO CELIAS/SEM EUV measurements saturated by extreme solar flare events. *Astronomische Nachrichten*, 328(1), 36-40. doi: 10.1002/asna.200610667
- Dominique, M., Hochedez, J.-F., Schmutz, W., Dammasch, I. E., Shapiro, A. I., Kretschmar, M., ... BenMoussa, A. (2013). The LYRA Instrument On-board PROBA2: Description and In-Flight Performance. *Solar Physics*, 286(1), 21-42. doi: 10.1007/s11207-013-0252-5
- Donnelly, R. F. (1976). Empirical models of solar flare X ray and EUV emission for use in studying their E and F region effects. *Journal of Geophysical Research*, 81(25), 4745-4753. doi: 10.1029/JA081i025p04745
- DRAP Documentation. (2010). *Global D-region absorption prediction documentation, accessed September, 2018*. Retrieved from <https://www.swpc.noaa.gov/content/global-d-region-absorption-prediction-documentation>
- Eccles, J. V., Hunsucker, R. D., Rice, D., & Sojka, J. J. (2005). Space weather effects on midlatitude HF propagation paths: Observations and a data-driven D region model. *Space Weather*, 3(1). (S01002) doi: 10.1029/2004sw000094
- Fiori, R. A. D., Koustov, A. V., Chakraborty, S., Ruohoniemi, J. M., Danskin, D. W., Boteler, D. H., & Shepherd, S. G. (2018). Examining the potential of the Super Dual Auroral Radar Network for monitoring the space weather impact of solar X-ray flares. *Space Weather*. doi: 10.1029/2018sw001905
- Galkin, I. A., Reinisch, B. W., Huang, X., & Bilitza, D. (2012). Assimilation of GIRO data into a real-time IRI. *Radio Science*, 47(4). doi: 10.1029/2011RS004952
- Greenwald, R., Baker, K. B., Dudeney, J. R., Pinnock, M., Jones, T., Thomas, E., ... Yamagishi, H. (1995). Darn/Superdarn: A Global View of the Dynamics of High-Latitude Convection. *Space Science Reviews*, 71, 761-796. doi: 10.1007/BF00751350
- Hall, G. E., MacDougall, J. W., Moorcroft, D. R., St.-Maurice, J.-P., Manson, A. H., & Meek, C. E. (1997). Super Dual Auroral Radar Network observations of meteor echoes. *Journal of Geophysical Research: Space Physics*, 102(A7), 14603-14614. doi: 10.1029/97JA00517
- Hanser, F. A., & Sellers, F. B. (1996). Design and calibration of the GOES-8 solar x-ray sensor: the XRS. *Proc.SPIE*, 2812, 2812 - 2812-9. doi:

- 10.1117/12.254082
- Hargreaves, J. (2010). Auroral radio absorption: The prediction question. *Advances in Space Research*, 45(9), 1075 - 1092. doi: 10.1016/j.asr.2009.10.026
- Hochedez, J.-F., Schmutz, W., Stockman, Y., Schühle, U., Benmoussa, A., Koller, S., ... Rochus, P. (2006). LYRA, a solar UV radiometer on Proba2. *Advances in Space Research*, 37, 303-312. doi: 10.1016/j.asr.2005.10.041
- Hunsucker, R. D., & Hargreaves, J. K. (2002). *The High-Latitude Ionosphere and its Effects on Radio Propagation*. Cambridge University Press.
- ITU-R P.372-13. (2016, 09). *Recommendation ITU-R P.372-13. Radio noise*. Retrieved from <https://www.itu.int/rec/R-REC-P.372-13-201609-I/en>
- Kravtsov, Y., & Orlov, Y. (1983). Caustics, catastrophes, and wave fields. *Soviet Physics Uspekhi*, 26(12), 1038.
- Lawal, H. A., Lester, M., Cowley, S. W. H., Milan, S. E., Yeoman, T. K., Provan, G., ... Rabiou, A. B. (2018). Understanding the global dynamics of the equatorial ionosphere in Africa for space weather capabilities: A science case for AfrequaMARN. *Journal of Atmospheric and Solar-Terrestrial Physics*. doi: 10.1016/j.jastp.2018.01.008
- Lawson, C., & Hanson, R. (1995). *Solving least squares problems*. Society for Industrial and Applied Mathematics. doi: 10.1137/1.9781611971217
- Lemen, J., Title, A., Akin, D., Boerner, P., Chou, C., Drake, J., ... Waltham, N. (2012). The Atmospheric Imaging Assembly (AIA) on the Solar Dynamics Observatory (SDO). *Solar Physics*, 275(1), 17-40. doi: 10.1007/s11207-011-9776-8
- Liu, E. X., Hu, H. Q., Liu, R. Y., Wu, Z. S., & Lester, M. (2012). An adjusted location model for SuperDARN backscatter echoes. *Annales Geophysicae*, 30(12), 1769-1779. doi: 10.5194/angeo-30-1769-2012
- Machol, J., & Viereck, R. (2016, Jun 10). *GOES X-ray Sensor (XRS) Measurements*. https://www.ngdc.noaa.gov/stp/satellite/goes/doc/GOES_XRS_readme.pdf.
- Machol, J., Viereck, R., & Jones, A. (2016, Nov 08). *GOES EUVS Measurements*. https://www.ngdc.noaa.gov/stp/satellite/goes/doc/GOES_NOP_EUV_readme.pdf.
- Oinats, A., Nishitani, N., Ponomarenko, P., Berngardt, O., & Ratovsky, K. (2016). Statistical characteristics of medium-scale traveling ionospheric disturbances revealed from the Hokkaido East and Ekaterinburg HF radar data. *Earth, Planets and Space*, 68(1), 8. doi: 10.1186/s40623-016-0390-8
- Pederick, L. H., & Cervera, M. A. (2014). Semiempirical Model for Ionospheric Absorption based on the NRLMSISE-00 atmospheric model. *Radio Science*, 49(2), 81-93. doi: 10.1002/2013RS005274
- Ponomarenko, P., Iserhienrhien, B., & St.-Maurice, J.-P. (2016). Morphology and possible origins of near-range oblique HF backscatter at high and midlatitudes. *Radio Science*, 51(6), 718-730. doi: 10.1002/2016rs006088
- Ponomarenko, P., Nishitani, N., Oinats, A. V., Tsuya, T., & St.-Maurice, J.-P. (2015). Application of ground scatter returns for calibration of HF interferometry data. *Earth, Planets and Space*, 67(1), 138. doi: 10.1186/s40623-015-0310-3

- Ponomarenko, P., St.-Maurice, J.-P., Hussey, G., & Koustov, A. (2010). HF ground scatter from the polar cap: Ionospheric propagation and ground surface effects. *J. Geophys. Res.*, *115*, 10310. doi: 10.1029/2010JA015828
- Ponomarenko, P., & Waters, C. (2006). Spectral width of SuperDARN echoes: measurement, use and physical interpretation. *Annales Geophysicae*, *24*(1), 115–128. doi: 10.5194/angeo-24-115-2006
- Ribeiro, A. J., Ruohoniemi, J., Baker, J., Clausen, L. B. N., Greenwald, R., & Lester, M. (2012). A survey of plasma irregularities as seen by the mid-latitude Blackstone SuperDARN radar. *Journal of Geophysical Research: Space Physics*, *117*(A2), A02311. doi: 10.1029/2011ja017207
- Ribeiro, A. J., Ruohoniemi, J., Baker, J., Clausen, S., de Larquier, S., & Greenwald, R. (2011). A new approach for identifying ionospheric backscatter in midlatitude SuperDARN HF radar observations. *Radio Sci.*, *46*, RS4011. doi: 10.1029/2011RS004676
- Rogers, N. C., & Honary, F. (2015). Assimilation of real-time riometer measurements into models of 30 MHz polar cap absorption. *J. Space Weather Space Clim.*, *5*, A8. doi: 10.1051/swsc/2015009
- Sauer, H. H., & Wilkinson, D. C. (2008). Global mapping of ionospheric HF/VHF radio wave absorption due to solar energetic protons. *Space Weather*, *6*(12). (S12002) doi: 10.1029/2008sw000399
- Schumer, E. A. (2010). *Improved modeling of midlatitude D-region ionospheric absorption of high frequency radio signals during solar X-ray flares* (Ph.D. dissertation). Air Force Institute of Technology.
- Shearman, E. D. R. (1956). A study of ionospheric propagation by means of ground back-scatter. *Proceedings of the IEE - Part B: Radio and Electronic Engineering*, *103*(8), 203-209. doi: 10.1049/pi-b-1.1956.0145
- Shepherd, S. G. (2017). Elevation angle determination for SuperDARN HF radar layouts. *Radio Science*, *52*(8), 938-950. (2017RS006348) doi: 10.1002/2017rs006348
- Simon, D. (2013). *Evolutionary Optimization Algorithms*. Wiley.
- Squibb, C. O., Frissell, N. A., Ruohoniemi, J. M., Baker, J. B. H., Fiori, R., & Moses, M. L. (2015). Dayside Ionospheric Response to X-Class Solar Flare Events Observed with Reverse Beacon Network High Frequency Communication Links. In *Virginia tech reu symposium – poster presentation*. Blacksburg, VA: Virginia Tech REU Program.
- Stocker, A. J., Arnold, N. F., & Jones, T. B. (2000). The synthesis of travelling ionospheric disturbance (TID) signatures in HF radar observations using ray tracing. *Annales Geophysicae*, *18*(1), 56–64. doi: 10.1007/s00585-000-0056-4
- Tinin, M. V. (1983). Propagation of waves in a medium with large-scale random inhomogeneities. *Radiophysics and Quantum Electronics*, *26*(1), 29–36. doi: 10.1007/BF01038771
- Tobiska, K. W., Bouwer, D. S., & Bowman, B. R. (2008). The development of new solar indices for use in thermospheric density modeling. *Journal of Atmospheric and Solar-Terrestrial Physics*, *70*(5), 803 - 819. doi: 10.1016/j.jastp.2007.11.001
- Uryadov, V. P., Vertogradov, G., Sklyarevsky, M. S., & Vybornov, F. I. (2018). Positioning of Ionospheric Irregularities and the Earth's Surface Roughness Using an Over-the-Horizon HF Radar. *Radiophysics and Quantum Electronics*. doi: 10.1007/s11141-018-9838-y

- Warrington, E., Stocker, A. J., Siddle, D. R., Hallam, J., Al-Behadili, H. A. H., Zaalov, N. Y., ... Danskin, D. (2016). Near real-time input to a propagation model for nowcasting of HF communications with aircraft on polar routes. *Radio Science*, 1048–1059. (2015RS005880) doi: 10.1002/2015rs005880
- Watanabe, D., & Nishitani, N. (2013). Study of ionospheric disturbances during solar flare events using the SuperDARN Hokkaido radar. *Advances in Polar Science*, 24(1), 12–18. doi: 10.3724/sp.j.1085.2013.00012
- Weisstein, E. (n.d.). *Parabolic Cylinder Function*. <http://mathworld.wolfram.com/ParabolicCylinderFunction.html>.
- Yukimatu, A. S., & Tsutsumi, M. (2002). A new SuperDARN meteor wind measurement: Raw time series analysis method and its application to mesopause region dynamics. *Geophysical Research Letters*, 29(20), 42-1-42-4. doi: 10.1029/2002GL015210